Available online at www.sciencedirect.com
SCIENCE DIRECT
Earth and Planetary Science Letters 248 (2006) 118–133
EPSL
www.elsevier.com/locate/epsl

Eocene to recent variations in erosion across the central Andean fold-thrust belt, northern Bolivia: Implications for plateau evolution

J.B. Barnes [a,*], T.A. Ehlers [a], N. McQuarrie [b], P.B. O'Sullivan [c], J.D. Pelletier [d]

[a] Department of Geological Sciences, University of Michigan, 2534 CCL Bldg., 1100 N. University Ave, Ann Arbor, MI 48109-1005, USA
[b] Department of Geosciences, M46 Guyot Hall, Princeton University, Princeton, NJ 08544, USA
[c] Apatite to Zircon, Inc., 1075 Matson Road, Viola, ID 83872-9709, USA
[d] Department of Geosciences, University of Arizona, 1040 E. 4th St., Tucson, AZ 85721, USA

Received 18 January 2006; received in revised form 16 May 2006; accepted 16 May 2006
Available online 7 July 2006
Editor: S. King

Abstract

Quantifying the erosional and kinematic evolution of orogenic plateaus has been limited by insufficient age constraints on their deformation and erosion histories. Palinspastic restorations suggest the central Andean fold-thrust belt and plateau evolved concurrently in Bolivia. We present an analysis that synthesizes 19 new and 32 previous apatite and zircon fission-track and (U–Th)/He mineral cooling ages along a 200 km traverse across the plateau margin and entire thrust belt in northern Bolivia. The new apatite fission-track data are interpreted using a grain-age deconvolution algorithm with inverse thermal modeling of track lengths, grain ages and mineral composition proxy data. Results suggest: (1) Eo-Oligocene (~40–25 Ma) initial rapid erosion of the plateau margin, (2) accelerated, distributed erosion across the entire thrust belt since the early to mid-Miocene (~15 Ma), and (3) the magnitude of erosion decreases eastward from ~10 to 4 km. We compare these results with two end-member models of the central Andes that contrast in duration and magnitude of deformation. The rapid Eo-Oligocene (~40–25 Ma) erosion is only consistent with the end-member that emphasizes the long duration and large magnitude deformation controlled by the sequential stacking of basement thrust sheets. However, the distributed Miocene (~15 Ma) to recent erosion is consistent with both end-members because the recorded cooling could have resulted from active deformation, protracted erosion or both. If the long duration model is correct, the time between the two phases of accelerated cooling brackets the cessation of the first basement thrust sheet and implies the early development of the Andean plateau analogous to its modern width, but unknown elevation by the early Miocene (~20 Ma).

Keywords: Andes; Bolivia; plateau; thermochronology; apatite fission track

1. Introduction

Many active mountain ranges are characterized by fold-thrust belts that exhibit significant relief, deformation and erosion. In the central Andes and the Himalayas, the hinterland portions of the thrust belts are occupied by high elevated plateaus characterized by unusually low relief and internal drainage [1–3]. The Andean and Tibetan plateaus are invoked to force global climate, Cenozoic climate change, terrestrial sediment flux and even ocean chemistry [4–6]. Despite their significance, observational constraints on plateau formation mechanisms across the entire width of

* Corresponding author. Tel.: +1 734 764 3431; fax: +1 734 763 4690.
E-mail address: barnesja@umich.edu (J.B. Barnes).

0012-821X/$ - see front matter © 2006 Elsevier B.V. All rights reserved.
doi:10.1016/j.epsl.2006.05.018

their marginal thrust belts are lacking. Nevertheless, proposed mechanisms for plateau formation prescribe a wide range of kinematic predictions from uniform plateau uplift to outward growth from a narrow orogenic belt [5,7].

The timing of formation of these large plateaus also remains unresolved (e.g. [8,9]). In particular, estimates on timing and rate of Andean plateau (AP) formation are based on a wide variety of proxies for plateau formation and elevation. These estimates are highly varied and range from ~40 to 5 Ma [1,9–19]. Thus, quantifying the timing and mechanisms of plateau development necessitates detailed regional knowledge of their deformation and erosion histories.

Erosion is the primary mechanism of exhumation in fold-thrust belts. In active tectonic settings such as the central Andes, the initial stages of accelerated erosion can also be a signature of deformation. For example, the relief generated by deformation is often what begins to drive the erosion process [20–25]. Low-temperature thermochronometers quantify rock exhumation in the shallow (upper 2–10 km) crust (e.g. [26]). In this study, we (1) quantify the spatial and temporal patterns of erosion across a 200 km transect through the entire northern Bolivian thrust belt by integrating new apatite fission-track (AFT) and zircon (U–Th)/He (ZHe) data with previous AFT and zircon fission-track (ZFT) data (Fig. 1), and (2) evaluate how these erosion patterns correlate with two models for the timing and kinematics of AP formation.

2. Geologic setting

The central Andean fold-thrust belt is divided into four physiographic regions (Fig. 1). These regions (after [27]) are: the Altiplano, Eastern Cordillera, Interandean zone and Subandes (Fig. 1A). The AP occupies the hinterland portion of the thrust belt and is defined as the broad region of low relief above 3 km elevation that encompasses both the Altiplano and the westernmost Eastern Cordillera (e.g. [1]). The physiographic regions are defined by large structural steps that correlate with an eastward down-stepping in average topographic elevation (Fig. 2A) [28]. The structural steps are basement highs that define the regional boundaries and play fundamental roles in the thrust belt structure [27–29]. The exposed rocks involved in the deformation range from Paleozoic marine siliciclastics to Mesozoic non-marine clastics and Tertiary synorogenic deposits (Fig. 1B) (e.g. [28,30]). Although the regional structure is important, correlations between along-strike variations in topography, climate and thrust belt geometry have been used to propose that the latitudinal erosion gradient also exerts a first-order control on the evolution of the plateau margin [31–33].

3. Previous work

In northern Bolivia, previous fission-track studies targeted predominantly Triassic plutons of the Eastern

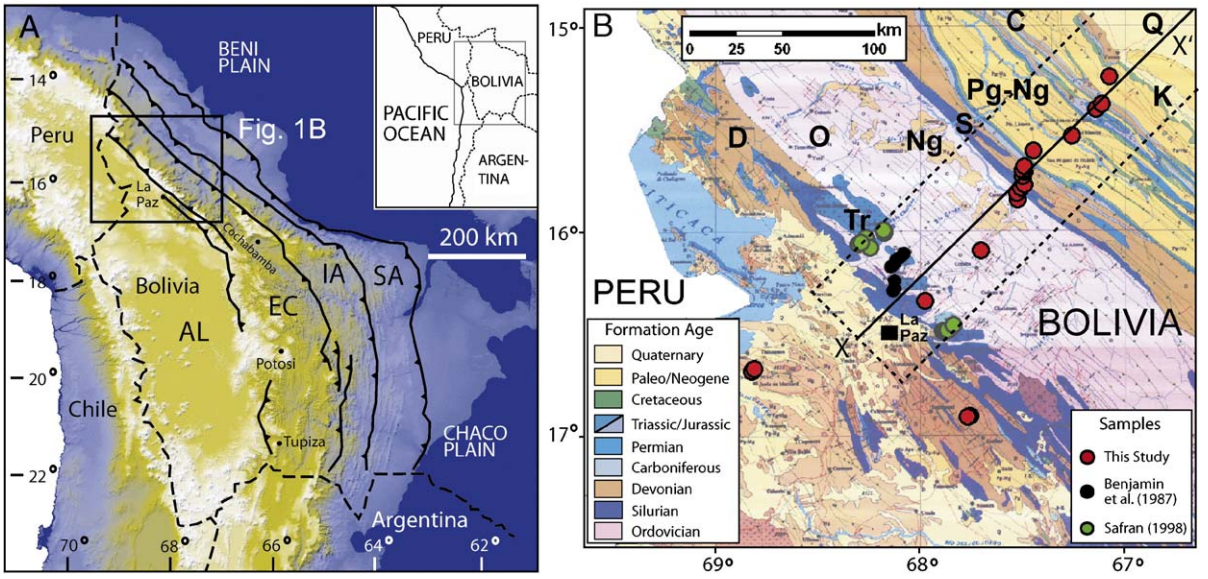

Fig. 1. The central Andean fold-thrust belt and plateau in Bolivia. (A) Major zones: AL=Altiplano, EC=Eastern Cordillera, IA=Interandean zone, SA=Subandes. Zone-bounding faults from McQuarrie [28]. (B) Regional geologic map (from [30]) with thermochronometer sample locations. Age of rock units are D=Devonian, O=Ordovician, S=Silurian, C=Carboniferous, Tr=Triassic, K=Cretaceous, Pg=Paleogene, Ng=Neogene, Q=Quaternary. X–X′ is transect line in Figs. 2, 4 and 5. Dashed rectangle is the extent of the swath-averaged topography plotted in Figs. 2 and 4A.

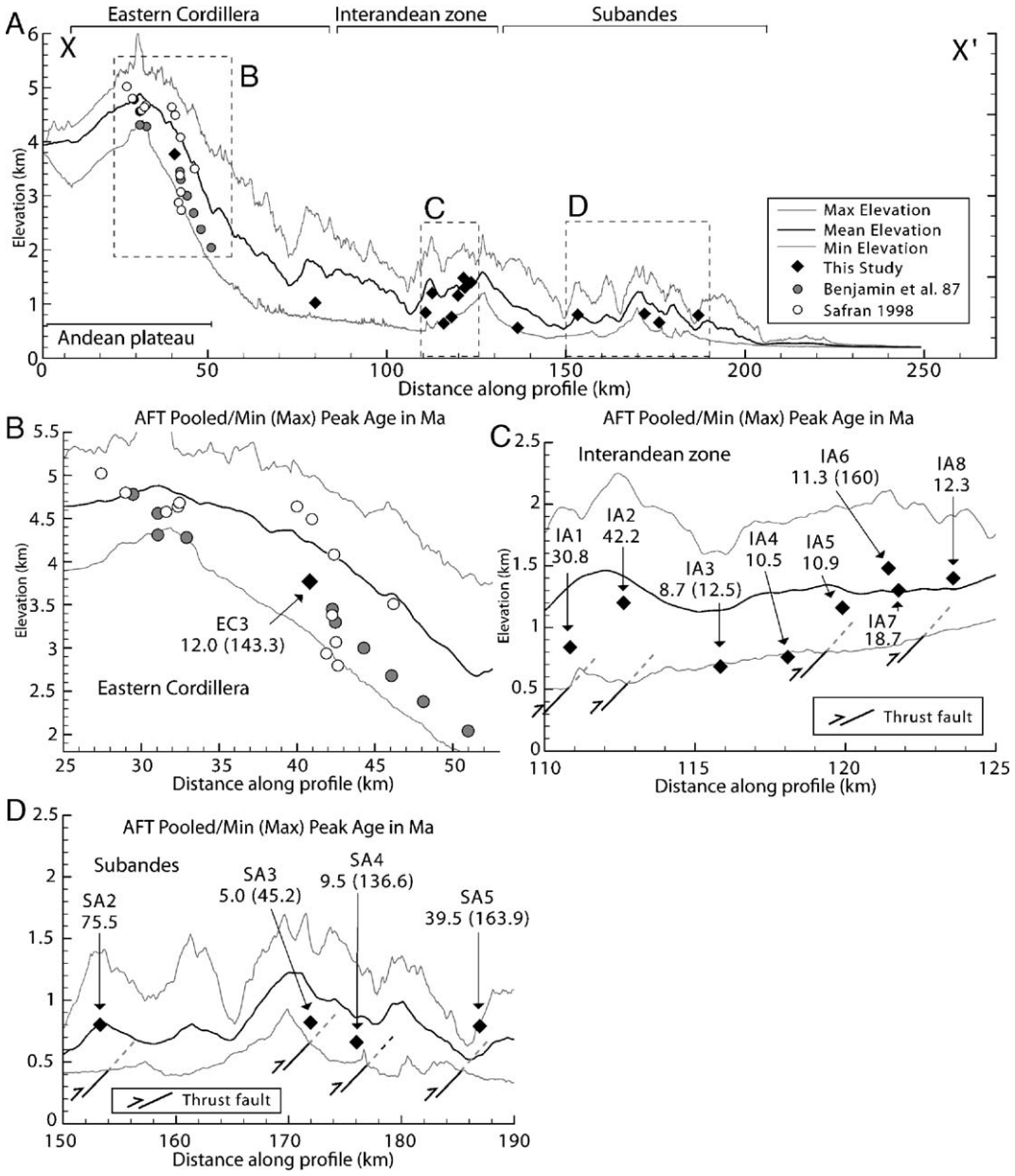

Fig. 2. Topography, structure and new apatite fission-track cooling ages across the fold-thrust belt. (A) 70-km wide swath-averaged minimum, mean and maximum topography profiles with projected sample locations. Topography from 90 m SRTM data. Profile location in Fig. 1B. Enlargements of the Eastern Cordillera (B), Interandean zone (C) and Subandes (D) show sample locations, IDs and AFT pooled age or Min (Max) component ages in Ma relative to mapped structures.

Cordillera which are limited to a narrow region of the plateau margin (Figs. 1 and 2) [16,30,34,35]. More recently, combined U–Pb, $^{40}Ar/^{39}Ar$, AFT and ZFT data of some of the same and adjacent plutons shows erosion-related exhumation with two rapid phases in the Eo-Oligocene and late Miocene to present totaling ~10 km in magnitude [36]. These aforementioned cooling histories have been used to indicate that shortening began ~40 Ma in the northern Eastern Cordillera [9,28]. Northern Subandes deformation is inferred to be Neogene from limited ages constraints on the foreland basin chronostratigraphy and structure [15,37,38]. Unfortunately, no constraints exist on the timing and amount of long-term exhumation for most of the northern thrust belt that extends ~150 km eastward from the plateau margin [39]. This study presents new thermochronometer data from

across the entire northern Bolivian thrust belt at 15–16°S (Fig. 1).

4. Methods

Apatite and zircon fission-track thermochronology utilizes the thermally sensitive retention of ^{238}U fission-generated damage trails in those minerals to constrain sample thermal histories [40–42]. Zircon (U–Th)/He thermochronology uses the accumulation of ^{4}He from the alpha decay of ^{238}U, ^{235}U and ^{232}Th in zircon crystals [43]. Although cooling rate and composition dependant, fission tracks in apatite generally become stable and record time since cooling through ~110 °C [44] which is commonly referred to as the closure temperature [45]. The closure temperature for ZHe is ~180 °C [46] and ~240 °C for ZFT [47]. Additionally, fission tracks experience length reduction (annealing) and ^{4}He can be lost by diffusion through temperatures significantly lower than their closure temperature (i.e. ~110–50 °C for AFT). This temperature region where the tracks are annealed or ^{4}He is lost is known as the partial annealing/retention zone ([48] and references therein).

AFT analytical results from sedimentary rock samples can exhibit significant variance because individual apatite grains possess non-uniform sources and cooling histories (see further discussion in Appendix B). We interpret the AFT data using the chi-square (χ^2) test [49,50], a statistical deconvolution of sample grain-age distributions [51–53], and inverse thermal modeling of the age, track lengths and mineral composition proxy data [54]. In brief, we (1) use the χ^2 test and grain-age distribution analysis results to identify the significant pooled or component age (s) in each sample grain-age distribution, and (2) use the results to guide placement of thermal constraints on the inverse modeling of each samples AFT data (see Appendix B). These two tools are combined to constrain the full range of possible onset times for the most recent rapid cooling history of each sample.

We use the following terminology to discuss sample AFT grain-age distribution analysis and interpretation. The χ^2 test classifies a grain-age distribution as either concordant ($P(\chi^2)>5\%$) or discordant ($P(\chi^2)<5\%$) [49,50]. Concordant samples have one significant component age that is geologically relevant and equivalent to the pooled age. Discordant samples have more than one significant component age and the pooled age is considered geologically meaningless [47]. In the discordant case, one must use the central age [55] or better yet identify (1) the minimum component age which not only constrains the most recent cooling, but is also the most easily resolved [47], and (2) the older component age(s) as it(or they) may signify cooling associated with either a more thermally resistant apatite composition end-member (i.e. Cl-apatite) and/or the source region [47,56]. Once the component age(s) have been identified, their age(s) relative to the sample depositional age allows the sample to be categorized (after [47]) as follows: reset samples contain one age component that is younger than the depositional age, and hence the grains have been reset to a younger age. Mixed reset samples contain multiple age components younger than the depositional age that have all been reset since deposition. Partially reset samples contain age components that are both younger and older than the depositional age such that only some of the grain ages were reset. Detrital samples have component ages older than deposition and hence have ages inherited from the source region.

ZHe analytical results can similarly exhibit significant variance because individual zircon grains can possess non-uniform sources and cooling histories as well as variable U and Th zonation, degrees of radiation damage and abrasion during transport ([57] and references therein). Regardless, in general, ZHe grain ages similarly represent either the age of rock cooling if it is younger

Table 1
Sample data

Sample zone/ID	Sample #	S Lat. (WGS84)	W Long. (WGS84)	Elev (m)	Fm age	Dist (m)
AL1	B811-1	−16.682	−68.818	3900	Pe	NA
AL2	B811-4	−16.668	−68.807	4450	Tert	NA
EC1	B721-5	−16.902	−67.766	2320	Sil	NA
EC2	B721-2	−16.896	−67.752	2240	L Dv	NA
EC3	725-13	−16.333	−67.974	3770	Ord	40.8
EC4	JB01-K3	−16.087	−67.701	1020	Ord	80.0
IA1	JB01-L3	−15.840	−67.521	840	Ord	110.8
IA2	JB01-M1	−15.803	−67.525	1200	Ord	112.6
IA3	JB01-M4	−15.783	−67.503	600	Sil	115.8
IA4	JB01-M7	−15.766	−67.489	760	U Sil	118.1
IA5	JB01-M8	−15.723	−67.497	1160	U Sil	119.9
IA6	JB01-N1	−15.697	−67.497	1480	U Dv	121.6
IA7	722-20	−15.704	−67.489	1301	L Dv	121.8
IA8	JB01-N2	−15.676	−67.487	1400	U Dv	123.7
SA1	JB01-N3	−15.596	−67.441	522	Tert	136.5
SA2	721-14	−15.526	−67.257	801	Jr	153.3
SA3	JB01-04	−15.395	−67.137	820	U Dv	171.9
SA4	JB01-06	−15.370	−67.108	640	Jr	176.0
SA5	JB01-09	−15.235	−67.072	790	Jr	186.9

Elev=elevation, Fm age=formation age, Pe=Precambrian, Tert=Tertiary, Sil=Silurian, Dv=Devonian, Ord=Ordovician, Jr=Jurassic, L=Lower, U=Upper, Zone=major zones, see Fig. 1; AL=Altiplano, EC=Eastern Cordillera, IA=Interandean zone, SA=Subandes; Dist= distance along profile in Figs. 2 and 4, NA=not applicable.

Table 2
Apatite fission-track data

Sample ID	ρ_s (10^6 tracks/cm^2)	N_s (tracks)	ρ_i (10^6 tracks/cm^2)	N_i (tracks)	ρ_d (10^6 tracks/cm^2)	N_d (tracks)	n	Dpar (μm)	Dper (μm)	P (χ^2) (%)	Pooled age (Ma±2σ)	Component ages (N_g) (Ma)	MTL±1σ (N_t) (μm) (tracks)	Desig
AL1	0.162	162	3.960	3949	4.233	4040	25	1.65	0.45	10.0	9.87±1.68	4.2 (4), 11.4 (21)	14.09±0.13 (115)	MR
AL2	0.141	169	0.907	1088	4.225	4040	40	2.20	0.61	0.0	37.2±6.6	8.7 (16), 58.6 (24)	11.82±0.21 (200)	PR
EC1	0.055	26	5.057	2382	4.242	4040	38	1.65	0.48	2.7	2.63±1.06	2.8±1.3 [a]	11.81±0.35 (69)	MR
EC2	0.038	7	1.897	346	4.250	4040	15	1.60	0.47	0.3	4.89±3.74	2.0 (13), 40.0 (2)	10.83±0.7 (14)	MR
EC3	0.352	60	0.792	135	3.720	4188	13	1.40	0.36	0.0	85.8±27	12.0 (11), 143.3 (2)	8.95±3.07 (24)	MR
EC4 [b]	0.385	16	0.601	25	2.783	4117	5	1.74	0.39	70.3	101±64	100.6 (5)	11.45±2.41 (3)	R
IA1 [b]	0.074	7	0.380	36	2.794	4117	7	1.63	0.47	52.8	30.8±25.6	30.8 (7)	14.27±0.93 (2)	R
IA2 [b]	0.244	30	0.920	113	2.805	4117	6	1.79	0.37	78.0	42.2±17.6	42.2 (6)	11.23 (1)	R
IA3	0.292	113	3.334	1291	2.816	4117	39	1.76	0.48	39.5	14.0±2.8	8.7 (14), 12.5 (25)	12.94±2.34 (79)	MR
IA4	0.29	66	4.420	1007	2.827	4117	32	1.78	0.45	92.5	10.5±2.8	10.5 (32)	13.32±1.78 (109)	R
IA5	0.262	109	3.877	1613	2.838	4117	40	1.80	0.41	64.5	10.9±2.2	10.9 (40)	13.46±2.03 (104)	R
IA6	0.308	166	4.355	2344	2.860	4117	40	1.83	0.43	17.1	11.5±2.0	11.3 (39), 160.3 (1)	14.09±1.65 (116)	MR
IA7 [b]	0.246	17	2.127	147	2.849	4117	4	1.84	0.51	1.0	18.7±9.6	18.7 (4)	15.33±0.50 (3)	R
IA8	0.301	166	4.007	2208	2.871	4117	39	1.79	0.47	40.2	12.3±2.2	12.3 (39)	13.64±1.75 (120)	R
SA1	0.841	555	1.181	779	2.882	4117	34	2.25	0.60	0.0	116±14	30.9 (14), 181.0 (20)	11.93±1.90 (202)	D/PR
SA2 [b]	0.436	24	0.945	52	2.893	4117	4	1.89	0.66	18.1	75.5±37.6	75.5 (4)	11.97±3.04 (3)	R
SA3	0.175	254	5.183	7531	3.759	4188	40	1.43	0.31	0.0	6.62±0.92	5.0 (38), 45.2 (2)	13.02±2.74 (173)	MR
SA4	0.716	596	2.710	2256	3.746	4188	40	1.42	0.34	0.0	51.5±5.6	9.5 (31), 136.6 (9)	11.79±2.56 (202)	MR
SA5	1.308	841	2.773	1783	3.733	4188	40	1.51	0.36	0.0	91.4±9.4	39.5 (19), 163.9 (21)	10.69±2.05 (202)	PR

ρ_s=density (cm^{-2}) of spontaneous tracks; N_s=number of spontaneous tracks counted; ρ_i=density (cm^{-2}) of induced tracks; ρ_d=density (cm^{-2}) of tracks on the neutron fluence monitor (CN-1 glass); N_d=number of tracks counted in the dosimeter; n=number of grains counted; Dpar=is the mean maximum diameter of fission-track etch figures parallel to the c-axis; Dper=is the mean maximum diameter of fission-track etch figures perpendicular to the c-axis; $P(\chi^2)$=probability (%) of greater chi-squared; MTL=mean track length; N_t=number of track lengths measured; N_g=number of grains contributing to that component age; Desig=designation after Brandon et al. [47]; R=reset; MR=mixed reset; PR=partially reset; D=detrital.

[a] Central age reported because component ages were unresolvable.

[b] Excluded from Figs. 4 and 5 due to less than 10 measured grain ages and track lengths.

than the depositional age, or the age of source region cooling if the age is older than the depositional age.

5. Results and interpretations

We present 19 new AFT samples paired with 4 ZHe results from samples across the central Andean fold-thrust belt in northern Bolivia (Fig. 1). Samples were collected from a wide range in elevation from Precambrian to Tertiary quartzites and sandstones (Fig. 2). Table 1 lists essential sample information, Table 2 the AFT results, Table 3 the ZHe results and Appendix A details the analytical procedures.

Interpretations of sample grain-age distributions assume the pooled/central or minimum age represents the youngest apparent cooling age or event (following [47]). Furthermore, we bracket the onset time of the most recent accelerated cooling by (1) quantifying the range of acceptable or better fits of thermal histories resolved with modeling, and (2) identifying the portion of resolved cooling histories where the particular sample cooled below AFT-sensitive temperatures (detailed in Appendix B). Fig. 3 shows representative examples of the component age analysis and thermal modeling results. Fig. 4 illustrates the distribution of all reliable cooling ages along the thrust belt transect. We group

Table 3
Zircon (U–Th)/He data

Sample ID[a]	Raw age (Ma)	Error (2σ)	Corrected (Ma)	Error (2σ)	U (ppm)	Th (ppm)	He (ncc/mg)	Ft
EC3a	11.84	0.44	15.72	0.59	445.10	413.07	781.93	0.75
EC3b	15.24	0.73	20.62	0.99	351.12	125.69	707.27	0.74
EC3c	25.40	6.17	33.35	8.10	54.17	18.14	181.09	0.76
SA3a	316.15	7.26	367.51	8.44	276.06	194.45	12783.77	0.86
SA3b	231.54	5.86	274.98	6.96	201.92	106.55	6548.73	0.84
SA3c	285.39	6.92	349.19	8.47	478.03	187.84	18695.17	0.82
SA4a	500.17	19.83	660.12	26.17	393.37	203.08	28383.85	0.76
SA4c	160.32	7.65	219.79	10.49	367.34	411.95	9189.97	0.73
SA5b	211.68	72.83	296.79	102.11	70.90	38.04	2101.56	0.71
SA5c	222.41	67.05	333.14	100.42	112.72	127.12	3940.26	0.67

σ=sigma, ppm=parts per million, ncc/mg=nanocubic centimeters per milligram, Ft=Ft correction factor.
[a] 2–3 grains, labeled a, b and/or c were measured for each sample.

observations and interpretations by physiographic region, moving eastward from the Altiplano.

5.1. Altiplano

Two AFT samples (AL1-2) were collected in the Altiplano ~85 km west of La Paz, Bolivia (Fig. 1B). The pooled AFT ages are 9.87 Ma and 37.2 Ma with mean track lengths (MTLs) of 14.09 and 11.82 μm, respectively. Sample AL1 from Precambrian sandstone is interpreted as mixed reset with AFT component ages of 11.4 and 4.2 Ma (Table 2). Sample AL2 from Tertiary sandstone is interpreted as partially reset with AFT component ages of 58.6 and 8.7 Ma. Collectively, these two samples show accelerated cooling from ~18 to 2 Ma which includes the 2σ error of the component ages from sample AL1.

5.2. Eastern Cordillera

We report four new AFT samples (EC1–4) from the Eastern Cordillera. Pooled AFT ages range from 101 to 2.6 Ma with MTLs of 11.81–8.95 μm. Component and central ages range from 143.3 to 2.0 Ma. The AFT samples are interpreted as partially reset, mixed reset and reset (Table 2).

Two samples were collected to the southeast of La Paz significantly separated from the main transect in Devonian and Silurian sandstones exposed within the La Paz river basin (Fig. 1B). Sample EC1 is reset with irresolvable component ages, so we report the central age (2.8 Ma) which is nearly identical to the pooled age (2.6 Ma) (Table 2). Sample EC2 is mixed reset with component ages of 40.0 and 2.0 Ma with the majority of the grains contributing to the minimum age component.

Along the main transect, sample EC3 (km 40.8, Fig. 2B) is consistent with protracted cooling from as early as ~40 Ma (Figs. 3A and 4C), though a minimum component age of 12 Ma implies more rapid cooling since <25 Ma. Sample EC4 (km 80.0, Fig. 2A) has a pooled age of 101 Ma, but <10 measured grain ages and track lengths. This precludes proper resolving of any component age populations (see Appendix B) and provides very limited modeling constraint on its recent cooling history (Fig. 3B). In summary, most of the reset AFT component ages record accelerated cooling from ~20 to 5 Ma. Additionally, previous work reported twenty-five AFT samples from the Eastern Cordillera (Figs. 1, 2A,B and 4C) [16,34]. The AFT ages range from 20 to 4.9 Ma (Fig. 4C). Unfortunately, neither χ^2 test results nor track-length measurements were reported for these samples [34,58]. In summary, AFT ages from the Eastern Cordillera are 25–2 Ma indicating accelerated cooling at this time (Fig. 4C) and are consistent with new AFT ages reported by [36]. At 1σ uncertainty, the Eastern Cordillera samples indicate accelerated cooling from ~21 to 3 Ma (Fig. 5).

One ZHe sample, EC3 (km 40.8, Fig. 4B), has relatively young (33–16 Ma) grain ages that we consider reset and roughly Oligo-Miocene or younger (Table 3). The large age range in the zircons insinuates they were either zoned or experienced partial ^{4}He loss. The same sample AFT component ages show a dominant young component at 12 Ma and a minor old component at 143 Ma (Table 2). A strong correlation between grain age (but not track length) and Dpar (2.9–2.7 μm for the old peak grains vs. <1.7 μm for the young peak grains) implies resetting of the only the less resistant apatites ([60]) and thus time spent in the partial annealing zone, consistent with a short MTL of 8.95 μm. We conclude that the 33–16 Ma ZHe grain

ages either (1) must be circumspect since they have a higher closure temperature, but have younger ages than the older component AFT age, or perhaps (2) the measured apatites were of the mixed F/OH Tiago variety [59] that overlaps in partial annealing/retention zone temperatures with ZHe [46]. A more detailed interpretation of the ZHe ages is not possible without additional analyses to characterize the grain-age variability.

Additionally, previous work reported seven ZFT ages ranging from 101 to 24.8 Ma with rapid exhumation interpreted to start ~40 Ma (Fig. 4B) [16,58]. The ZFT ages are older than the ZHe ages in the Eastern Cordillera, as would be expected due to its sensitivity to higher temperatures (Fig. 4B). The three oldest (101–68 Ma) ZFT ages were interpreted to result from significant time spent in the zircon partial annealing zone before rapid cooling began at ~40 Ma as recorded by the younger (~50–29 Ma) ZFT ages (Fig. 4B) [16].

5.3. Interandean zone

Eight samples (IA1–8) were collected from four different thrust sheets in the Interandean zone (Fig. 2C). Pooled AFT ages range from 42.2 to 10.5 Ma and MTLs from 14.27 to 11.23 μm. Minimum and old component ages range from 11.3 to 8.7 Ma and 160.3 to 12.5 Ma, respectively. All samples are designated as reset and mixed reset (Table 2).

Low grain yields from samples IA1 and IA2 (km 110.8 and 112.6, Fig. 2C) have limited model-constrained recent cooling from between 31–10 Ma and 52–3 Ma, respectively. Sample IA3 (km 115.8, Fig. 4C) shows constrained accelerated cooling from >~100 °C temperatures from as early as ~20 Ma (Fig. 4C) consistent with its pooled age of 14 Ma and its component ages of 12 and 9 Ma (Fig. 3C). Samples IA4 (km 118.1), IA5 (km 119.9) and IA8 (km 123.7) all passed the χ^2 test and show constrained cooling associated with their pooled ages ranging from 12.3 to 10.5 Ma (Figs. 3D and 4C). Sample IA6 has two component ages of 160.3 and 11.3 Ma, but the minimum age is nearly identical to the pooled age of 11.5±2.0 Ma. Modeling shows the acceptable cooling histories within the error associated with the minimum component age estimate (Fig. 4C). Sample IA7 (km 121.8, Fig. 2C) possesses a low number of grain ages and track lengths measured and modeling does not further constrain its recent cooling history beyond its pooled age of 18.7± 9.6 Ma. In summary, the good quality data have young component ages from ~18 to 3 Ma and indicate rapid cooling starting from ~15 to 5 Ma at the 1σ uncertainty (Figs. 4C and 5).

5.4. Subandes

Five samples (SA1–5) were collected from four different thrust sheets in the Subandes (Fig. 2A and C). Pooled AFT ages range from 116 to 6.6 Ma with MTLs of 13.02–10.69 μm. Minimum component ages range from 39.5 to 5 Ma and old component ages range from 181 to 45.2 Ma. These samples are designated as reset, mixed reset, partially reset and detrital (Table 2).

We interpret sample SA1 (km 136.5, Fig. 2A) as either detrital or partially reset because it is from Tertiary sandstone and has component ages of 181 and 30.9 Ma. Without further depositional age control, we cannot discern if the young age component is older or younger than the depositional age. However, the larger grain contribution to the Mesozoic age component shows that there is a significant detrital cooling signal in this sample (Table 2). Note the acceptably fit recent cooling from ~100 °C since ~41–11 Ma as recorded by the minimum component age and modeling (Fig. 3E). This recent cooling follows significant time in the apatite partial annealing zone from ~140 to 40 Ma (Fig. 3E) as corroborated by a short MTL of 11.93 μm.

Sample SA2 (km 153.3, Fig. 2D) has a pooled age of 75.5 Ma and poorly constrained model results with cooling commencing as early as ~110 Ma. This may reflect a lower magnitude of cooling on this structure compared to others, or a poorly resolved cooling history due to the low number of grains (<10 grains) analyzed. Samples SA3 and SA4 (km 171.9, 176.0, Fig. 2D) are mixed reset with minimum component ages and modeling indicating recent rapid cooling from ~19–4 Ma (Fig. 4C).

Sample SA5 (km 186.9, Fig. 4C) is Jurassic sandstone and considered partially reset because it has component ages of 163.9 and 39.5 Ma. The minimum component age, though reset, is unusually old

Fig. 3. Representative grain-age distributions and modeled thermal histories from the thrust belt transect apatite fission-track data. (I) BinomFit [52] results showing grain-age histogram (bars), probability density function fit to the grain-age distribution (line) and binomially best-fit component age (s) (thick lines labeled with age). Abbreviations are the same as in Fig. 1 and Table 2. AFTSolve [54] results showing permissible thermal histories (II) and measured versus modeled track length distributions (III). Thermal histories shown are acceptable (light gray), good (dark gray) and the best (black line), with imposed model constraints (vertical bars). Numbers are the pooled ages (age) and mean track lengths (MTL) with 1σ, number of grain ages or track lengths measured (*N*), and goodness of fit (GOF) between the model results and the data for both the age and MTL data [61]. Histograms in (III) show measured (in binned bars) and best-fit model (solid line) track length distributions.

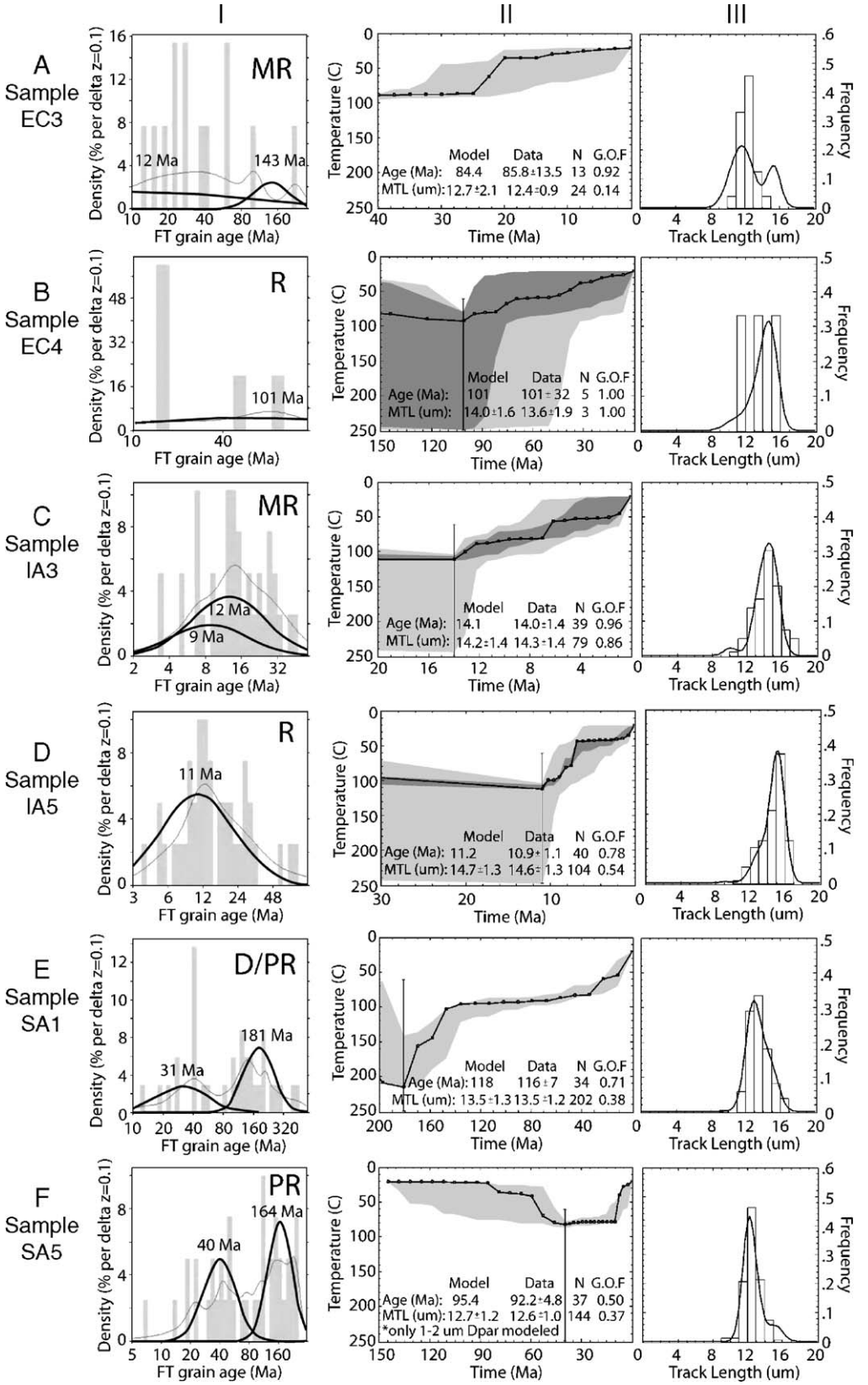
I
II
III
A
Sample
EC3
MR
12 Ma
143 Ma
Density (% per delta z=0.1)
FT grain age (Ma)
Temperature (C)
Time (Ma)
Track Length (um)
Frequency
Model Data N G.O.F
Age (Ma): 84.4 85.8±13.5 13 0.92
MTL (um): 12.7±2.1 12.4±0.9 24 0.14
B
Sample
EC4
R
101 Ma
Model Data N G.O.F
Age (Ma): 101 101±32 5 1.00
MTL (um): 14.0±1.6 13.6±1.9 3 1.00
C
Sample
IA3
MR
12 Ma
9 Ma
Model Data N G.O.F
Age (Ma): 14.1 14.0±1.4 39 0.96
MTL (um): 14.2±1.4 14.3±1.4 79 0.86
D
Sample
IA5
R
11 Ma
Model Data N G.O.F
Age (Ma): 11.2 10.9±1.1 40 0.78
MTL (um): 14.7±1.3 14.6±1.3 104 0.54
E
Sample
SA1
D/PR
31 Ma
181 Ma
Model Data N G.O.F
Age (Ma): 118 116±7 34 0.71
MTL (um): 13.5±1.3 13.5±1.2 202 0.38
F
Sample
SA5
PR
40 Ma
164 Ma
Model Data N G.O.F
Age (Ma): 95.4 92.2±4.8 37 0.50
MTL (um): 12.7±1.2 12.6±1.0 144 0.37
*only 1-2 um Dpar modeled

considering that it is from the easternmost structure of the Subandes, which is believed to have been active for only the last ~10 Ma (e.g. [17]). Unfortunately, no acceptable modeled cooling histories fit the data when either both component ages or only the minimum age is used as a constraint for the cooling history and no correlation exists between Dpar and grain age. Furthermore, there are no acceptable cooling histories when the grains are grouped into generic fluorapatite (2–1 μm Dpar) and chlorapatite (3–2 μm Dpar) kinetic populations with their respective track-length distributions [60,61]. The only way to achieve any acceptable thermal histories is to model only the most thermally sensitive population of fluorapatite (2–1 μm Dpar, MTL 12.6 μm) grains using a thermal event at 40 Ma, as constrained by the minimum component age [47,61]. This result suggests accelerated cooling from apatite partial annealing zone temperatures of ~80 °C or more from between ~19 and 4 Ma (Figs. 3F and 4C). The protracted time this sample spent in the partial annealing zone prior to rapid cooling is corroborated by a short MTL of 10.69 μm (Table 2). In summary, most of the Subandes samples have young component ages from 30 to 5 Ma that record accelerated cooling starting from ~19 to 4 Ma (Fig. 4C). At 1σ uncertainty level, it appears rapid cooling began ~12–5 Ma (Fig. 5).

From west to east, three Subandes samples with ZHe analyses have ages of 368–275 Ma, 660–220 Ma and 333–297 Ma, respectively (Fig. 4B). We simply interpret these ZHe ages as partially reset for sample SA3 from Upper Devonian rocks and detrital for samples SA4 and SA5 from Jurassic units (Table 3). A more detailed interpretation of these sample ZHe ages is not possible without additional analyses to characterize the nature of the range in the ages.

6. Discussion and implications

Thermochronometer ages represent the time since cooling below closure. Combined with additional information, such as track-length distributions and kinetic parameters in apatite, cooling histories can be constrained with modeling. Thermochronometer cooling can result from either igneous activity, tectonic exhumation (i.e. normal faulting) or erosion [48,62]. According to the latest mapping, lack of evidence for proximal (<~50 km) Tertiary intrusions/volcanism near the samples in northern Bolivia, as well as significant normal faulting allows the inference that recorded cooling was the result of erosional exhumation [36,63]. Similar to other studies (see, for example, [20–25]), we assume that the early stages of erosion-driven exhumation are the result of deformation because thrust faulting facilitates erosion by generating topography and relief. This assumption still recognizes that erosion-related cooling can continue long after deformation has ceased. Thus, thermochronometer data from thrust belts can be sensitive to the onset time of deformation, but poorly constrain when deformation terminates due to protracted erosional exhumation. This highlights the need for future work to address how erosion rates and magnitudes change across structures during and after deformation.

We first highlight the spatial and temporal variations in cooling due to erosion across the thrust belt and compare them with two end-member deformation models. We next estimate the spatial and temporal distribution of erosion magnitudes using constraints on the subsurface thermal field from borehole data. Finally, we briefly compare thermochronologic results from across the entire AP from Peru to Argentina.

6.1. Erosion and plateau development

The observed erosion patterns tend to be broad and most easily defined by the various physiographic zones. Fig. 5 summarizes the regional spatial and temporal trends in cooling ages and the onset of accelerated ZFT-and-AFT-recorded cooling across the thrust belt. The Altiplano and Eastern Cordillera has ZFT ages from 50 to 29 Ma and AFT ages from 25 to 2 Ma that record accelerated erosion from ~40 to 25 Ma and from ~15 Ma (or younger) to the present [16,36]. The Interandean zone has AFT ages from 18 to 3 Ma that record accelerated erosion since ~15 Ma. The westernmost Subandes have AFT ages that record erosion from 41–11 Ma related to the Eastern Cordillera to the west, whereas most of the Subandes experienced accelerated erosion from ~19 to 4 Ma that could be as recent as ~5 Ma. The distribution of erosion documented by the thermochronometer data across the thrust belt highlights two major trends: (1) initial onset of accelerated erosion ~40 Ma in the Eastern Cordillera, followed by (2) synchronous rapid erosion across the entire plateau and thrust belt since ~15 Ma.

As outlined in [9], there are two end-member deformation models for the evolution of the central Andes. A short duration and low-magnitude shortening characterizes one end-member that describes predominately Neogene deformation occurring in two stages [1,10,15,17,64]: (1) distributed deformation in the Altiplano and Eastern Cordillera began at ~27 Ma, followed by (2) deformation concentrated exclusively in the Subandes since ~10 Ma. A long duration and large-magnitude shortening characterizes the other end-member that emphasizes higher magnitudes

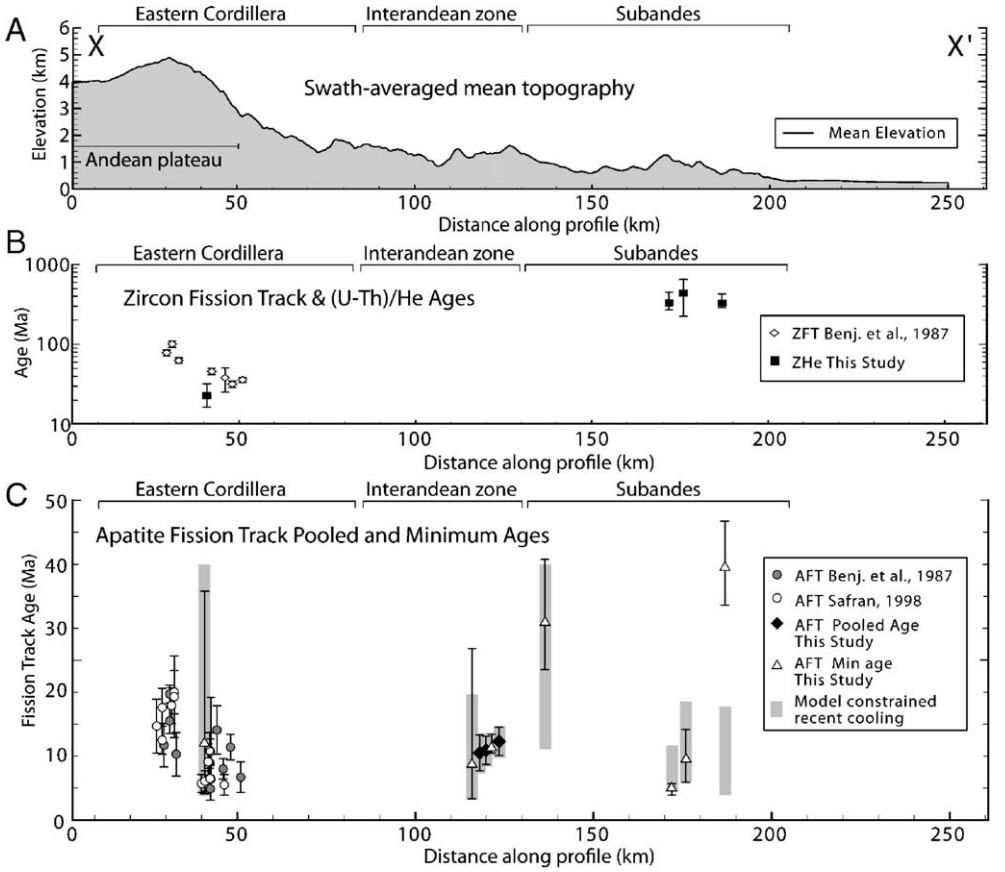

Fig. 4. Mean topography and robust thermochronometer cooling ages across the fold-thrust belt. See Fig. 1B for location. (A) 70-km wide swath-averaged mean elevation. (B) ZFT and ZHe ages. Error bars are 2σ for the ZFT. ZHe symbols are plotted on the sample average age (bars show range of grain ages). Note the semilog scale. (C) AFT pooled or minimum component ages for samples with >10 measured grains and/or track lengths. Error bars are 2σ. Gray bars are the age range for the onset of the most recent cooling constrained by modeling.

of shortening and the role of basement-involved deformation [9,12,28,65]. Although the exact geometry of the basement deformation is unknown (compare [28,66]), the deformation chronologies are similar (see also [67]). This model describes Eocene deformation in the Eastern Cordillera propagated by bi-vergent deformation moving west towards the Altiplano and eastward to the Subandes where it has been concentrated since the early to late Miocene.

If the first end-member model is applicable, we would expect erosion from ~27 to 10 Ma or less in the Altiplano and Eastern Cordillera (which includes the Interandean zone in this model) followed by erosion from ≤~10 Ma in the Subandes. The ZFT cooling in the Eastern Cordillera from ~40 to 25 Ma reveals earlier Eocene pre-27 Ma deformation, uplift and erosion. Furthermore, the model-constrained AFT-cooling from as early as 19 Ma in the Subandes suggests deformation and erosion began in the region before 10 Ma (Fig. 5). However, the fact that accelerated cooling in the Subandes could be as recent as ~12–5 Ma is consistent with this model.

If the second end-member model is applicable, we would expect erosion beginning in the Eastern Cordillera in the Eocene followed by more recent erosion both westwards and eastwards to the present. The Eocene erosion ~40–25 Ma is consistent with the eastward propagation of an upper-basement thrust over a ramp beneath the Eastern Cordillera [28,29]. Additional evidence corroborates this model by limiting deformation in this region from post mid-Paleocene to pre late-Oligocene [11,12,36]. The distributed erosion since ~15 Ma is consistent with the emplacement of a second, lower-basement thrust that began ≤~20 Ma ([28,29], see also [68]). This lower-basement thrusting is responsible for uplifting the Interandean zone with respect to the foreland, transferring slip eastward into the Subandes, and possibly deforming the Altiplano through basement duplexing. In other words, the young accelerated erosion (<~15 Ma) in the Eastern Cordillera was not contemporaneous with deformation on surface structures in this region [36]. Instead, the ~15–2 Ma

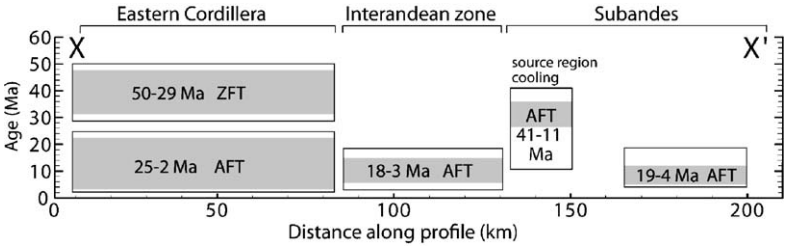

Fig. 5. Spatial and temporal variations in erosion recorded by thermochronometer ages across the fold-thrust belt. Boxes and labels are the robust cooling age ranges (2σ) further constrained by modeling after Fig. 4. ZFT = zircon fission track, AFT = apatite fission track. Sample EC3 95% CI range for the young age component excluded due to extremely large error. Gray regions show 1σ range in ages.

accelerated cooling must be erosionally driven while early to late Miocene deformation in the Altiplano [11] and Subandes initially drove the ~15 Ma erosion in those regions. We note that the ~15–5 Ma cooling ages in the Interandean zone is equally consistent with both end-member models signifying deformation and erosion began in this region at this time.

Shortening associated with the upper-basement thrust is recognized to be responsible for most of the present crustal thickness and presumably some of the AP elevation [28]. The accelerated erosion ~40–25 Ma in the Eastern Cordillera probably records movement of the upper-basement thrust sheet. If the distributed erosion since ~15 Ma records motion of the lower basement shortening, then it follows that the upper-basement thrust sheet must have ceased between 25 and 15 Ma. Therefore, we infer the early development of the AP analogous to its modern width and near present day crustal thickness at ~20 Ma. However, evidence from leaf physiognomy and paleoerosion surface remnants implies that much of the modern elevation of the AP came later in the late Miocene [14,17]. The protracted cooling since ~15 Ma in the Altiplano and Eastern Cordillera is also consistent with late Miocene rapid surface uplift [19].

In summary, the two regional cooling events suggested by the thermochronometer data have the following implications for the contending deformation models of the central Andes: (1) the onset of erosion from ~40 to 25 Ma in the Eastern Cordillera is consistent with the longer duration model [28]; (2) synchronous erosion across the entire plateau and thrust belt since ~15 Ma is consistent with both models [1,17,28].

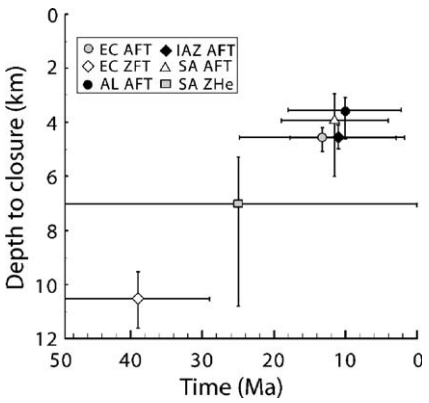

Fig. 6. Estimated erosion magnitudes across the fold-thrust belt. Symbols are located at the median cooling age for each region and horizontal error bars represent the range in regional cooling ages after Fig. 5. Vertical bars represent the range in erosion magnitude due to the percent error in the heat flow measured thermal gradients. See Figs. 1 and 4 for abbreviations.

6.2. Spatial distribution of erosion magnitude

We estimated erosion magnitudes across the thrust belt using measured thermal gradients and effective closure temperatures [59] for each thermochronometer system to calculate the depth to closure. This effectively allows quantification of the amount of material removed since the samples cooled below their closure temperatures (Fig. 6). We assume average closure temperatures of 110 °C for AFT, 180 °C for ZHe and 240 °C for ZFT, and average surface temperatures of 10 °C for the Altiplano and Eastern Cordillera, 15 °C for the Interandean zone and 23 °C for the Subandes [44,46,47,69,70]. Proximal borehole-measured geothermal gradients and estimates of mean surface temperatures combine to represent the best-available proxy for the thermal field through which the samples cooled. Our selection criteria for borehole-estimated thermal gradients include: (1) measurement reliability, (2) location within the same physiographic province as the samples, (3) application of a topographic correction and (4) location within one crustal thickness distance (~55–45 km [71]) of sample locations to minimize regional variations in basal heat flux that might alter near surface thermal gradients. However, in some cases, the measurements we use

are not as proximal because the borehole data are sparse and sometimes unreliable.

In the Altiplano, we use a thermal gradient of 27 °C/km ±20% error. This value comes from the only reliable measurement located at Chacarilla, ~115 km from our two samples [72]. We estimate ~3.7 km of erosion in the Altiplano since ~18–2 Ma from the AFT component ages (Fig. 6). In the Eastern Cordillera, we use a gradient of 22 °C±10% at Chojilla. Chojilla is at most ~50 km from our samples and ~75 km from all previously reported Eastern Cordillera samples [72]. The Eastern Cordillera thermal gradient could be less than that observed in the Altiplano due to the large topographic effect from the high relief (>2 km) (Fig. 2A). We estimate ~10.6 km erosion since ~40–25 Ma from the ZFT data and ~4.6 km since ~15–5 Ma from the AFT data (Fig. 6). These estimates are a refinement of previous work that assumed a generic thermal gradient of 30 °C/km [16,36,73]. We assume the same gradient for the Interandean zone. The Chojilla station is at most ~90 km from all Interandean samples. We estimate ~4.6 km of erosion since ~15–5 Ma from the AFT data (Fig. 6).

No proximal thermal gradient measurements exist for our samples in the northern Subandes. However, a large compilation of over 1500 measurements from the southern Subandes and adjacent Chaco basin yields a mean gradient of 22.4 °C±~35% with a mean surface temperature of 23 °C±10% from robust linear regression [69]. Assuming these values for the northern Subandes, the erosion magnitude is limited to ≤~7.0 km from the mostly detrital ZHe ages since at least ~220 Ma and estimated to be ~3.9 km since ~15–5 Ma from the AFT data (Fig. 6).

Estimated erosion magnitudes decrease eastward across the thrust belt (Fig. 6). The Eastern Cordillera ZFT and ZHe ages are young in contrast to the ZHe ages of the Subandes. The Subandes ZHe ages consist of a dominantly detrital signal inherited from Paleozoic to early Mesozoic times and are presumably not associated with Andean orogenesis. The detrital to partially reset Subandes ZHe ages combined with the reset AFT components from the same samples bracket the magnitude of erosion in the Subandes. The Subandes structures have been eroded from AFT-sensitive temperatures (~110 °C), but not from ZHe-sensitive temperatures (~180 °C). The mostly detrital Tertiary foreland basin sample from the western Subandes (km 136.5, Fig. 4C) suggests the local amount of erosion since deposition and burial has been limited to less than AFT-sensitive temperatures. The modeling constrained cooling from 41 to 11 Ma (Fig. 5) is therefore presumably associated with deformation and erosion of the hinterland structures in the Eastern Cordillera.

One additional observation is the extremely young AFT central and component ages (2.8–2.0 Ma) collected from low elevations within the high relief La Paz basin just south of our transect (Fig. 1B). The late Pliocene ages suggests that the basin has experienced rapid recent fluvial incision by the La Paz River in conjunction with its headward erosion into the Altiplano.

6.3. Along-strike variation in Andean plateau erosion

Along-strike exhumation of the Andean plateau suggests non-uniform deformation and erosion from as early as the late Eocene to as recent as the late Miocene. North of this study, K–Ar and $^{40}Ar/^{39}Ar$ AFT ages record late Eocene exhumation with continued Oligo-Miocene exhumation recorded by AFT ages in Peru [74]. As summarized in this paper, AFT ages in northern Bolivia show Eocene to late Oligocene accelerated erosion in the Eastern Cordillera followed by widespread Miocene (~15 Ma) to recent accelerated erosion. In southern Bolivia, AFT ages in the AP are Oligocene (~30 Ma), mid-Miocene (17–9 Ma) in the Interandean zone and late Mio-Pliocene in the Subandes [75]. Farther south in Argentina, AFT-recorded exhumation of the Puna plateau is Oligo-Miocene [20,21].

7. Conclusions

Low-temperature thermochronology across the central Andean fold-thrust belt in northern Bolivia reveal a two-phased erosion history. Accelerated erosion began in the Eastern Cordillera in the Eo-Oligocene (~40–25 Ma), followed by distributed, accelerated erosion since the early–mid-Miocene (~15 Ma). The magnitude of erosion decreases eastward from ~10.6 km in the Eastern Cordillera, to ~4.6 km in the Interandean zone and to between ~3.9 and ~7.0 km in the Subandes. Models for the kinematic evolution of the central Andean plateau must be consistent with these spatial and temporal trends in erosion, their magnitudes, and associated and inferred deformation. Assessment of two end-member models for central Andean deformation show the following: the earlier Eo-Oligocene phase of erosion is consistent with one model that highlights earlier deformation controlled by the sequential stacking of basement thrusts. However, the distributed erosion since ~15 Ma is equally consistent with both end-member models of deformation that predict deformation and erosion in the Interandean zone and Subandes in the early to late Miocene. If the basement-involved deformation model is correct, the time between the two phases of accelerated cooling brackets the cessation of the first basement thrust and implies

establishment of the AP analogous to its modern width, but unknown elevation by the early Miocene (~20 Ma).

Acknowledgements

We thank Sergiotecmin of La Paz, Bolivia and especially Sohrab Tawackoli for logistical support. We thank Ken Farley for access to his lab for the ZHe analyses. J. Barnes recognizes advice by Andy Carter in interpreting the AFT data. Mark Brandon helped with the BinomFit analyses as well as reviewed an earlier version of the manuscript. Reviews by J. Garver and S. Thomson improved this paper. Support was provided to T.A. Ehlers by NSF grant EAR 0409289.

Appendix A. AFT and ZHe analytical procedures

A.1. AFT data

Apatite grains were separated using conventional heavy-liquid and magnetic separation techniques, etched and irradiated by Apatite to Zircon, Inc. using the external detector method and irradiation facilities at the Nuclear Radiation Center, Washington State University. For standardization, a mica sheet was attached to a ^{235}U-doped CN-1 glass and the reactor operated at 1 MW power output yielding a thermal-neutron fluence of approximately 10^{16} neutrons/cm^2. Apatite grain mounts were polished following immersion in epoxy resin cured at 90 °C for 1 h. Apatite mounts were immersed in 5.5 N HNO_3 at 21 °C (±1 °C) for 20.0 s (±0.5 s), whereas the mica sheets were immersed in 48% HF for 15 min (±15 s) at 20 °C (±1 °C). Additional apatite mounts were irradiated by a ^{252}Cf source in a vacuum to enhance the measurability of natural fission tracks [76]. Only natural, horizontal, and confined tracks were measured for both length (±0.2 μm) and the angle to the *c*-axis (±2°). The FT analyses were performed at 2000× magnification under un-polarized light. We conducted age calculations for samples JB01-04, JB01-06, JB01-09 and 725-13 (Table 1) from apatite standards of the Fish Canyon Tuff, USA, and Cerro de Mercado, Durango, Mexico with a personal zeta calibration factor of 104.5±2.6 (1σ) (for PBO). For all other samples, a zeta calibration factor of 113.8±2.9 (1σ) (for RAD) was used from the same apatite standards. Table 2 details the AFT analytical results.

Age and track-length measured apatite grains were classified for annealing kinetics with the parameter Dpar. Dpar is defined as the fission-track etch pit diameter parallel to the c-axis of the apatite crystal at the polished and etched surface of the analyzed grain [60]. For each grain measured for age or track length, we recorded between 1 and 4 Dpar values and determined a mean Dpar.

A.2. ZHe data

Zircon separates from some of the samples were sieved to 100–150 μm minimum dimensions. Grains were hand-picked under a 120× binocular microscope, measured to determine the α emission correction [77] for the crystallographic *a*- and *b*-axes, loaded into Pt capsules, and out gassed under a Nd-YAG laser at ~1350 °C for 15 min. Evolved helium was spiked with ^{3}He, cryogenically concentrated and purified, and the ^{4}He/^{3}He ratio measured on a quadrupole mass spectrometer. Laser re-extracts of grains yielded no measurable ^{4}He. After outgassing, grains were retrieved, digested, spiked with ^{235}U and ^{230}Th, and the U and Th isotope ratios analyzed by ICP-MS. The propagated 1σ analytical uncertainty on these He ages is ~2% [78]. Table 3 details the ZHe data.

Appendix B. AFT data interpretation methodology

In this appendix, we summarize the relevant principals to sedimentary sample AFT grain-age distribution analysis and detail our thermal modeling methodology.

B.1. Sedimentary AFT grain-age distribution analysis

AFT analytical results from sedimentary units often exhibit significant variance because individual apatites are more likely to have experienced different thermal histories before being incorporated into the sampled depositional unit. In other words, if the sedimentary unit has not been completely reset since deposition, the inherited, variable thermal histories of the individual apatite grains may contribute to a large range in measured AFT cooling ages and track lengths (e.g. [60]). Furthermore, individual apatite grains are likely to have different sources and hence different compositions. Composition influences the annealing behavior of apatite (e.g. [56]). Therefore, the post-depositional, shared cooling history experienced by all grains in a sample will result in different measured grain ages and track lengths among the grains.

The chi-square (χ^2) test evaluates the variance of a sample grain-age distribution [49,50]. Unfortunately, statistical reliability of the χ^2 test breaks down with a low number of measured spontaneous and induced fission tracks (N_s, N_i<5) [47]. Therefore, if a particular sample has very few tracks measured, it could have an inflated chi-square value and pass the $P(\chi^2)$ test appearing to be concordant when, in fact, it is discordant.

The AFT grain-age distributions can be analyzed using a deconvolution algorithm that identifies the statistically significant populations and their component ages within each sample [51]. If only one component age is identified,

it is equivalent to the pooled age. We used BinomFit [51–53] to identify the significant component ages in our samples. BinomFit calculates the individual grain ages and their uncertainties, and combines a binomial peak-fitting scheme with an iterative search to optimize the number of significant component ages in a sample [52].

B.2. Thermal modeling of AFT data

The grain-age distribution and component ages, track-length distribution and grain composition proxy data all combine to provide valuable information that can be used to constrain a samples thermal history with inverse modeling. We modeled the fission-track data with AFTSolve [54] which incorporates track length, grain age and composition proxy data. Fundamentally, AFTSolve uses various search methods to quantify the range of statistically acceptable and better thermal histories for a single sample that (1) adheres to user-defined constraints and (2) matches the measured data.

Overall, our modeling strategy started with an open-ended model with minimal constraints. We incrementally imposed restrictions directed by the successive modeling results and relevant geologic data, such as depositional age of the sampled formation and the sample pooled or component AFT age(s) [54]. We used a multi-kinetic annealing model which allows for modeling of multiple kinetic apatite populations with Dpar [79].

For the initial general model, we ran 15,000 simulations with a controlled random search (CRS) technique for each sample. All age and track-length data were modeled as one kinetic population projected to the c-axis in order to effectively remove the problems of anisotropic track-length reduction [80]. We imposed two main constraints [61]: (1) a starting temperature of 200 °C at an age equal to 1.5 times the pooled or maximum component age of the sample and (2) 20 °C at the present time. Both non-montonic and monotonic heating/cooling was explored with a rate not allowed to exceed 20–40 °C/My [61]. Any insights gained on the more recent portion of the sample cooling history were successively explored using a Monte Carlo search technique with additional constraints imposed on the recent portion of the sample cooling history as directed from the previous results. Only the monotonic cooling results are reported in this paper because in most cases the onset of recent cooling was not significantly different from the non-monotonic cases.

Refined modeling involved imposing additional constraints from the sample formation age and the component grain-age analysis results. 15,000 simulations were first run with all age and length data as one kinetic population using a Monte Carlo search. The constraints on each sample thermal history included: (1) the starting temperature was set to 20 °C at the approximate deposition age of the sample; (2) a temperature of 20 °C at the present time, as well as (3) a 60–250 °C temperature constraint at the pooled or youngest component age (this is a conservative temperature range that AFT data might be sensitive to at a potentially high rate of cooling during thrust sheet emplacement and hanging wall erosion). This setup was explored for the range of 1σ uncertainties in the pooled age or 68% CI (confidence interval) values (very similar to 1σ) in the youngest component age calculated by BinomFit. If the sample had a second age component, then that age was subsequently set as an additional 60–250 °C temperature constraint and similarly explored.

Even though many samples have discordant grain-age distributions, very few samples exhibited even moderate correlations between Dpar and grain age or track length. However, in all samples with two component ages, the kinetic populations were delineated and modeled together to identify the acceptable cooling histories for the sample. Additionally, the lower Dpar population (<2 μm) was modeled independently since it represents the most thermally sensitive group of grains [47]. These component age modeling efforts followed the methodology above. See [61] for additional discussion of the methodology for separating kinetic populations.

References

[1] B.L. Isacks, Uplift of the central Andean plateau and bending of the Bolivian Orocline, J. Geophys. Res. 93 (1988), 3211–3231.
[2] P. Tapponnier, X. Zhiqin, F. Roger, B. Meyer, N. Arnaud, G. Wittlinger, Y. Jingsui, Oblique stepwise rise and growth of the Tibetan plateau, Science 294 (2001), 1671–1677.
[3] E.R. Sobel, G.E. Hilley, M.R. Strecker, Formation of internally drained contractional basins by aridity-limited bedrock incision, J. Geophys. Res. 108 (2003), doi:10.1029/2002JB001883.
[4] F.M. Richter, D.B. Rowley, D.J. DePaolo, Sr isotope evolution of seawater: the role of tectonics, Earth Planet. Sci. Lett. 109 (1992), 11–23.
[5] L. Royden, Coupling and decoupling of crust and mantle in convergent orogens; implications for strain partitioning in the crust, J. Geophys. Res. 101 (1996), 17679–17705.
[6] W.F. Ruddiman, M.E. Raymo, W.L. Prell, J.E. Kutzbach, The uplift-climate connection; a synthesis, in: W.F. Ruddiman (Ed.), Tectonic Uplift and Climate Change, Plenum Press, New York, 1997, pp. 471–515.
[7] S. Wdowinski, Y. Bock, The evolution of deformation and topography of high elevated plateaus: 2. Application to the central Andes, J. Geophys. Res. 99 (1994), 7121–7130.
[8] M.A. Murphy, A. Yin, T.M. Harrison, S.B. Duerr, Z. Chen, F.J. Ryerson, W.S.F. Kidd, X. Wang, X. Zhou, Did the Indo-Asian collision alone create the Tibetan plateau? Geology 25 (1997), 719–722.
[9] N. McQuarrie, B.K. Horton, G. Zandt, S. Beck, P.G. DeCelles, Lithospheric evolution of the Andean fold-thrust belt, Bolivia,

and the origin of the central Andean plateau, Tectonophysics 399 (2005), 15–37.
[10] R.W. Allmendinger, T.E. Jordan, S.M. Kay, B.L. Isacks, The evolution of the Altiplano-Puna plateau of the central Andes, Annu. Rev. Earth Planet. Sci. 25 (1997), 139–174.
[11] S. Lamb, L. Hoke, Origin of the high plateau in the central Andes, Bolivia, South America, Tectonics 16 (1997), 623–649.
[12] B.K. Horton, Revised deformation history of the central Andes: inferences from Cenozoic foredeep and intermontane basins of the Eastern Cordillera, Bolivia, Tectonics 24 (2005), doi:10.1029/2003TC001619.
[13] L. Kennan, S.H. Lamb, L. Hoke, High-altitude palaeosurfaces in the Bolivian Andes; evidence for late Cenozoic surface uplift, in: M. Widdowson (Ed.), Palaeosurfaces; Recognition, Reconstruction and Palaeoenvironmental Interpretation, Geological Society of London, 1997, pp. 307–323.
[14] K.M. Gregory-Wodzicki, Uplift history of the central and northern Andes; a review, Geol. Soc. Amer. Bull. 112 (2000), 1091–1105.
[15] T. Sempere, G. Herail, J. Oller, M.G. Bonhomme, Late Oligocene–early Miocene major tectonic crisis and related basins in Bolivia, Geology 18 (1990), 946–949.
[16] M.T. Benjamin, N.M. Johnson, C.W. Naeser, Recent rapid uplift in the Bolivian Andes; evidence from fission-track dating, Geology 15 (1987), 680–683.
[17] T.L. Gubbels, B.L. Isacks, E. Farrar, High-level surfaces, plateau uplift, and foreland development, Bolivian central Andes, Geology 21 (1993), 695–698.
[18] P.G. DeCelles, B.K. Horton, Early to middle Tertiary foreland basin development and the history of Andean crustal shortening in Bolivia, Geol. Soc. Amer. Bull. 115 (2003), 58–77.
[19] C.N. Garzione, P. Molnar, J. Libarkin, B. MacFadden, Rapid late Miocene rise of the Bolivian Altiplano: evidence for removal of mantle lithosphere, Earth Planet. Sci. Lett. 241 (2006), 543–556.
[20] T.J. Coughlin, P.B. O'Sullivan, B.P. Kohn, R.J. Holcombe, Apatite fission-track thermochronology of the Sierras Pampeanas, central western Argentina; implications for the mechanism of plateau uplift in the Andes, Geology 26 (1998), 999–1002.
[21] B. Carrapa, D. Adelmann, G.E. Hilley, E. Mortimer, E.R. Sobel, M.R. Strecker, Oligocene range uplift and development of plateau morphology in the southern central Andes, Tectonics 24 (2005), doi:10.1029/2004TC001762.
[22] E.R. Sobel, M.R. Strecker, Uplift, exhumation and precipitation: tectonic and climatic control of late Cenozoic landscape evolution in the northern Sierras Pampeanas, Argentina, Basin Res. 15 (2003), 431–451.
[23] S. Willett, Orogeny and orography; the effects of erosion on the structure of mountain belts, J. Geophys. Res. 104 (1999), 28957–28982.
[24] S. Willett, M. Brandon, On steady states in mountain belts, Geology 30 (2002), 175–178.
[25] M.K. Clark, M.A. House, L.H. Royden, K.X. Whipple, B.C. Burchfiel, X. Zhang, W. Tang, Late Cenozoic uplift of southeastern Tibet, Geology 33 (2005), 525–528.
[26] T.A. Ehlers, K.A. Farley, Apatite (U–Th)/He thermochronometry; methods and applications to problems in tectonic and surface processes, Earth Planet. Sci. Lett. 206 (2003), 1–14.
[27] J. Kley, Geologic and geometric constraints on a kinematic model of the Bolivian Orocline, J. South Am. Earth Sci. 12 (1999), 221–235.
[28] N. McQuarrie, The kinematic history of the central Andean fold-thrust belt, Bolivia; implications for building a high plateau, Geol. Soc. Amer. Bull. 114 (2002), 950–963.
[29] J. Kley, Transition from basement-involved to thin-skinned thrusting in the Cordillera Oriental of southern Bolivia, Tectonics 15 (1996), 763–775.
[30] H.P. Guarachi, S. Tawackoli, W.A. Salinas, H.M. Gonzales, Mapa Geologico de Bolivia, Servicio Geologico de Bolivia/YPFB, La Paz, Bolivia, scale 1:1,000,000, 2001.
[31] S. Lamb, P. Davis, Cenozoic climate change as a possible cause for the rise of the Andes, Nature 425 (2003), 792–797.
[32] B.K. Horton, Erosional control on the geometry and kinematics of thrust belt development in the central Andes, Tectonics 18 (1999), 1292–1304.
[33] D.R. Montgomery, G. Balco, S.D. Willett, Climate, tectonics, and the morphology of the Andes, Geology 29 (2001), 579–582.
[34] E.B. Safran, Channel network incision and patterns of mountain geomorphology, PhD, University of California at Santa Barbara, 1998.
[35] S.T. Crough, Apatite fission-track dating of erosion in the eastern Andes, Bolivia, Earth. Planet. Sci. Lett. 64 (1983), 396–397.
[36] R.J. Gillis, B.K. Horton, M. Grove, Thermochronology, geochronology, and upper crustal structure of the Cordillera Real: Implications for Cenozoic exhumation of the central Andean plateau, Tectonics (in press).
[37] D. Roeder, R.L. Chamberlain, Structural geology of sub-Andean fold and thrust belt in northwestern Bolivia, in: A.J. Tankard, R. Suarez, H.J. Welsink (Eds.), Petroleum Basins of South America, AAPG Memoir, vol. 62, 1995, pp. 459–479.
[38] D. Roeder, Andean-age structure of Eastern Cordillera (Province of La Paz, Bolivia), Tectonics 7 (1988), 23–39.
[39] J.B. Barnes, J.D. Pelletier, Latitudinal variation of denudation in the evolution of the Bolivian Andes, Am. J. Sci. 306 (2006), 1–31.
[40] T. Tagami, Zircon fission-track thermochronology and application to fault studies, in: P.W. Reiners, T.A. Ehlers (Eds.), Low-Temperature Thermochronology: Techniques, Interpretations, and Applications, Reviews in Mineralogy and Geochemistry, vol. 58, MSA, Chantilly, VA, 2005, pp. 95–122.
[41] T. Tagami, P.B. O'Sullivan, Fundamentals of fission-track thermochronology, in: P.W. Reiners, T.A. Ehlers (Eds.), Low-Temperature Thermochronology: Techniques, Interpretations, and Applications, Reviews in Mineralogy and Geochemistry, vol. 58, MSA, 2005, pp. 19–47.
[42] R.A. Donelick, P.B. O'Sullivan, R.A. Ketcham, Apatite fission-track analysis, in: P.W. Reiners, T.A. Ehlers (Eds.), Low-Temperature Thermochronology: Techniques, Interpretations, and Applications, Reviews in Mineralogy and Geochemistry, vol. 58, MSA, Chantilly, VA, 2005, pp. 49–94.
[43] K.A. Farley, (U–Th)/He dating: techniques, calibrations, and applications, in: D. Portcelli, C.J. Ballentine, R. Wieler (Eds.), Noble Gases in Geochemistry and Cosmochemistry, Rev. in Mineral. Geochem., vol. 47, MSA, Washington, DC, 2002, pp. 819–843.
[44] K. Gallagher, R. Brown, C. Johnson, Fission track analysis and its applications to geological problems, Annu. Rev. Earth Planet. Sci. 26 (1998), 519–572.
[45] M.H. Dobson, Closure temperature in cooling geochronological and petrological systems, Contrib. Mineral. Pet. 40 (1973), 259–274.
[46] P.W. Reiners, T.L. Spell, S. Nicolescu, K.A. Zanetti, Zircon (U–Th)/He thermochronometry: He diffusion and comparisons with 40Ar/39Ar dating, Geochim. Cosmochim. Acta 68 (2004), 1857–1887.
[47] M. Brandon, M. Roden-Tice, J. Garver, Late Cenozoic exhumation of the Cascadia accretionary wedge in the Olympic

Mountains, Northwest Washington State, Geol. Soc. Amer. Bull. 110 (1998), 985–1009.
[48] K.V. Hodges, Geochronology and thermochronology in orogenic systems, in: R.L. Rudnick (Ed.), Treatise on Geochemistry, vol. 3, Elsevier Ltd., 2003, pp. 263–292.
[49] R.F. Galbraith, On statistical models for fission-track counts, J. Math. Geol. 13 (1981), 471–478.
[50] P.F. Green, A new look at statistics in fission-track dating, Nucl. Tracks Radiat. Meas. 5 (1981), 77–86.
[51] M.T. Brandon, Decomposition of fission-track grain-age distributions, Am. J. Sci. 292 (1992), 535–564.
[52] M.T. Brandon, Decomposition of mixed grain age distributions using BinomFit, On Track 24 (2002), 13–18.
[53] T.A. Ehlers, T. Chaudhri, S. Kumar, C.W. Fuller, S.D. Willett, R.A. Ketcham, M.T. Brandon, D.X. Belton, B.P. Kohn, A.J.W. Gleadow, T.J. Dunai, F.Q. Fu, Computational tools for low-temperature thermochronometer interpretation, in: P.W. Reiners, T.A. Ehlers (Eds.), Low-Temperature Thermochronology: Techniques, Interpretations, and Applications, Reviews in Mineralogy and Geochemistry, vol. 58, MSA, Chantilly, VA, 2005, pp. 589–622.
[54] R.A. Ketcham, R.A. Donelick, M.B. Donelick, AFTSolve; a program for multi-kinetic modeling of apatite fission-track data, Geol. Mat. Res. 2 (2000), 1–32.
[55] R.F. Galbraith, G.M. Laslett, Statistical models for mixed fission track ages, Nucl. Tracks Radiat. Meas. 21 (1993), 459–470.
[56] W.D. Carlson, R.A. Donelick, R.A. Ketcham, Variability of apatite fission-track annealing kinetics: I. Experimental results, Amer. Min. 84 (1999), 1213–1223.
[57] P.W. Reiners, Zircon (U–Th)/He thermochronometry, in: P.W. Reiners, T.A. Ehlers (Eds.), Low-Temperature Thermochronology: Techniques, Interpretations, and Applications, Reviews in Mineralogy and Geochemistry, vol. 58, MSA, Chantilly, VA, 2005, pp. 151–179.
[58] M.T. Benjamin, Fission Track Ages on Some Bolivian Plutonic Rocks; Implications for the Tertiary Uplift and Erosion History of the Altiplano-Cordillera Real, MS, Dartmouth College, 1986.
[59] P.W. Reiners, M.T. Brandon, Using thermochronology to understand orogenic erosion, Annu. Rev. Earth Planet. Sci. 34 (2006), 419–466.
[60] R.L. Burtner, A. Nigrini, R.A. Donelick, Thermochronology of Lower Cretaceous source rocks in the Idaho–Wyoming thrust belt, AAPG Bull. 78 (1994), 1613–1636.
[61] R.A. Ketcham, R.A. Donelick, AFTSolve version 1.3.0, Donelick Analytical, Inc. and Richard A. Ketcham, 2001.
[62] U. Ring, M. Brandon, S. Willett, G. Lister, Exhumation processes, in: U. Ring, M. Brandon, G. Lister, S. Willett (Eds.), Exhumation Processes; Normal Faulting, Ductile Flow and Erosion, vol. 154, Geol. Soc. London, London, 1999, pp. 1–27.
[63] Sergiomin, Mapas Tematicos de Recursos Minerales de Bolivia, Hojas La Paz y Copacabana, SE 19-2, Geobol, La Paz, Bolivia, scale 1:250,000, 1997.
[64] T.E. Jordan, J.H. Reynolds III, J.P. Erikson, Variability in age of initial shortening and uplift in the central Andes, in: W.F. Ruddiman (Ed.), Tectonic Uplift and Climate Change, Plenum Press, New York, 1997, pp. 41–61.
[65] N. McQuarrie, P.G. DeCelles, Geometry and structural evolution of the central Andean backthrust belt, Bolivia, Tectonics 20 (2001), 669–692.
[66] J.P. Muller, J. Kley, V. Jacobshagen, Structure and Cenozoic kinematics of the Eastern Cordillera, southern Bolivia (21°S), Tectonics 21 (2002), doi:10.1029/2001TC001340.
[67] K. Elger, O. Oncken, J. Glodny, Plateau-style accumulation of deformation: southern Altiplano, Tectonics 24 (2005), doi:10.1029/2004TC001675.
[68] R.W. Allmendinger, T.R. Zapata, The footwall ramp of the Subandean decollement, northernmost Argentina, from extended correlation of seismic reflection data, Tectonophysics 321 (2000), 37–55.
[69] M. Springer, A. Forster, Heat-flow density across the central Andean subduction zone, Tectonophysics 291 (1998), 123–139.
[70] Instituto Geografico Militar, Digital Atlas of Bolivia, La Paz, Bolivia, 2000, CDROM.
[71] S.L. Beck, G. Zandt, S.C. Myers, T.C. Wallace, P.G. Silver, L. Drake, Crustal-thickness variations in the central Andes, Geology 24 (1996), 407–410.
[72] S.G. Henry, H.N. Pollack, Terrestrial heat flow above the Andean subduction zone in Bolivia and Peru, J. Geophys. Res. 12 (1988), 15,153–15,162.
[73] J.G. Masek, B.L. Isacks, T.L. Gubbels, E.J. Fielding, Erosion and tectonics at the margins of continental plateaus, J. Geophys. Res. 99 (1994), 13,941–13,956.
[74] D.J. Kontak, E.A. Farrar, A.H. Clark, D.A. Archibald, Eocene tectono-thermal rejuvenation of an upper Paleozoic–lower Mesozoic terrane in the Cordillera de Carabaya, Puno, southeastern Peru, revealed by K–Ar and (super 40)Ar/(super 39) Ar dating, J. South Am. Earth Sci. 3 (1990), 231–246.
[75] H. Ege, E.R. Sobel, V. Jacobshagen, E. Scheuber, D. Mertmann, Exhumation history of the central Andes of southern Bolivia by apatite fission track dating, Rev. Tec. YPFB 21 (2003), 165–172.
[76] R.A. Donelick, D.S. Miller, Enhanced TINT fission track densities in low spontaneous track density apatites using 252Cf-derived fission fragment tracks: a model and experimental observations, Nucl. Tracks Radiat. Meas. 18 (1991), 301–307.
[77] K. Farley, R. Wolf, L. Silver, The effects of long alpha-stopping distances on (U–Th)/He ages, Geochim. Cosmochim. Acta 60 (1996), 4223–4229.
[78] K. Farley, Helium diffusion from apatite; general behavior as illustrated by Durango fluorapatite, J. Geophys. Res. 105 (2000), 2903–2914.
[79] R.A. Ketcham, R.A. Donelick, W.D. Carlson, Variability of apatite fission-track annealing kinetics: III. Extrapolation to geological time scales, Am. Mineral. 84 (1999), 1235–1255.
[80] R.A. Donelick, R.A. Ketcham, W.D. Carlson, Variability of apatite fission-track annealing kinetics: II. Crystallographic orientation effects, Am. Mineral. 84 (1999), 1224–1234.